Supplementary Information

Origin of discrete resistive switching in chemically heterogeneous vanadium oxide crystals

B. Raju Naik[1], Yadu Chandran[1], Kakunuri Rohini[1], Divya Verma[1], Shriram Ramanathan[2], Viswanath Balakrishnan[1]*

[1] School of Mechanical and Materials Engineering, Indian Institute of Technology Mandi, Himachal Pradesh-175075, INDIA.

[2]Department of Electrical and Computer Engineering, Rutgers State University, New Jersey, Piscataway, NJ 08854.

*Corresponding author email: viswa@iitmandi.ac.in

Table of Contents:

Figure S1. Atomic Force Microscopy (AFM) image and line profile across points A and B of VO_2 crystal.

Figure S2. I-V measurements of various VO_2 devices. (a-d) Device-1 to Device-4.

Figure S3. (a) Optical microscope image of VO_2 with bright and dark contrasts and (b) Raman spectra obtained from four neighbouring bright and dark regions of single crystal VO_2. The positions where the Raman spectrum was taken are marked with cross marks. The red cross marks correspond to bright, and the yellow corresponds to dark regions.

Figure S4. Energy dispersive x-ray spectroscopy (EDS) spectra from dark and bright regions of a VO_2 single crystal. It shows that V_nO_{2n-1} (bright region) intensity is nearly double that of VO_2 (dark region).

Figure S5. Differential scanning calorimetry (DSC) phase transition temperature analysis (a) DSC phase transition temperature plots. (b) IMT temperatures were recorded over 9 repeated cycles. Orange-colored pentagons show IMT temperatures of VO_2, and dark cyan colour triangles represent VnO_{2n-1}. (c) enthalpy changes as a function of a number of cycles.

Figure S6. (a) *In-situ* SEM I-V plots of single crystal from VO_2 and V_nO_{2n-1} regions. (b) load-displacement plots from V_nO_{2n-1} and VO_2 region, for fixed 400 μN load. (c) I-V plots from nano ECR measurement conducted on VO_2 in vertical geometry.

Figure S7. Figure shows the XPS V2p spectra depth analysis at different etching values of (a) 7 nm (b) 50 nm (c) 100 nm and (d) 200 nm respectively.

Figure S8. Optical microscopy images of single crystal VO_2 for studying the thermal heating and cooling effect on chemical heterogeneity dynamics. Metallic and insulating domains are marked with the letter's "M" and "I," respectively, near the transition temperature. Orange-coloured circled regions are interesting observations for bright and dark regions' motion at 25ºC, well below the transition temperature.

Figure S9. Optical microscopy images of single crystal VO_2 under heating conditions, showing dynamics in IMT domains.

Figure S10. The TEM bright field images and selected area electron diffraction pattern of VO_2 crystal in inset. (a) The lamellar-like microstructure was indicated by black arrow marks and moiré fringes marked with yellow arrow marks. (b) Microdomain like line contrasts are marked with white arrow marks. (c) Thick VO_2 platelet. Selected area electron diffraction patterns shown in insets comprise mixed reflections from VO_2 and other nonstoichiometric phases.

Figure S11. (a) Current as a function of electric field for a crystalline VO_2 sample at different temperatures (b) The electric field threshold dependence on temperature.

Figure S12. Current-voltage plots are depicted in red and blue for temperatures just below and just above the phase transition, respectively.

Figure S13. Depicts the XPS characterization of the Ar+H_2 annealed crystalline VO_2 sample. V2p spectra for (a) as grown VO_2 having +4 and +5 oxidation states (b) 15 min Ar+H_2 annealed sample with +3, +4 and +5 oxidation states (b) 30 min Ar+H_2 annealed sample with +3, +4 and +5 oxidation states (c) 45 min Ar+H_2 annealed sample with +3, +4 and +5 oxidation states (d) 60 min Ar+H_2 annealed sample with +3, +4 and +5 oxidation states and (e) 3D histogram representing distribution of oxidation state percentages from each sample.

Figure S14. Depicts the RT plots and discrete I-V switching curves. (a) RT plots for a as grown and different Ar+H_2 annealed time dependent samples under heating mode. I-V switching characteristics for (a) as grown samples with a multiple discrete stochastic switching having equal ΔV_{th} of 0.74 V (b) 15 min- Ar+H_2 annealed sample (c) 30 min Ar+H_2 annealed sample (d) 45 min Ar+H_2 annealed sample and (e) 60 min Ar+H_2 annealed sample with higher number of discrete thresholds switching to reduced number of discrete switching having different ΔV_{th} voltages.

Figure S15. Raman spectrum and the phase transition confirmation in polycrystalline VO_2. (a) Raman spectrum of PC-VO_2 (b) Thermal triggering of insulator-metal phase transition captured via R-T plot during heating (c) DSC confirmation for phase change in VO_2 (d) Electrical triggering induced phase change.

Table S1. The estimated values of change in free energy with respect to the composition of vanadium oxides and respective parameters used in redox reaction.

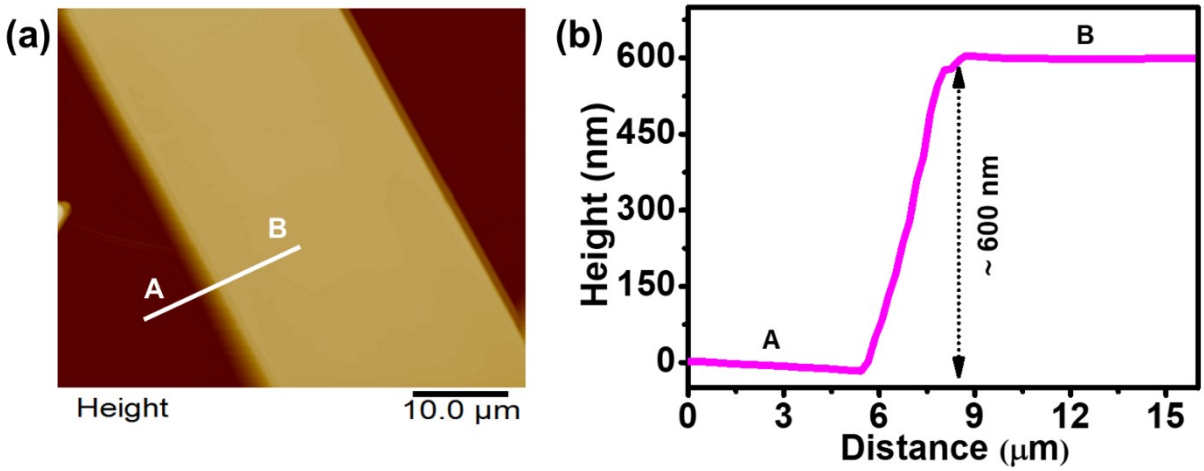

Figure S1. (a) Atomic Force Microscopy (AFM) image and (b) line profile across points A and B of VO_2 crystal.

AFM was employed to determine the thickness of VO_2 microcrystals, and we expect slight variations in thickness among the crystals of different lateral dimensions. The measured single crystal thickness was 600 nm (Figure S1a-b).

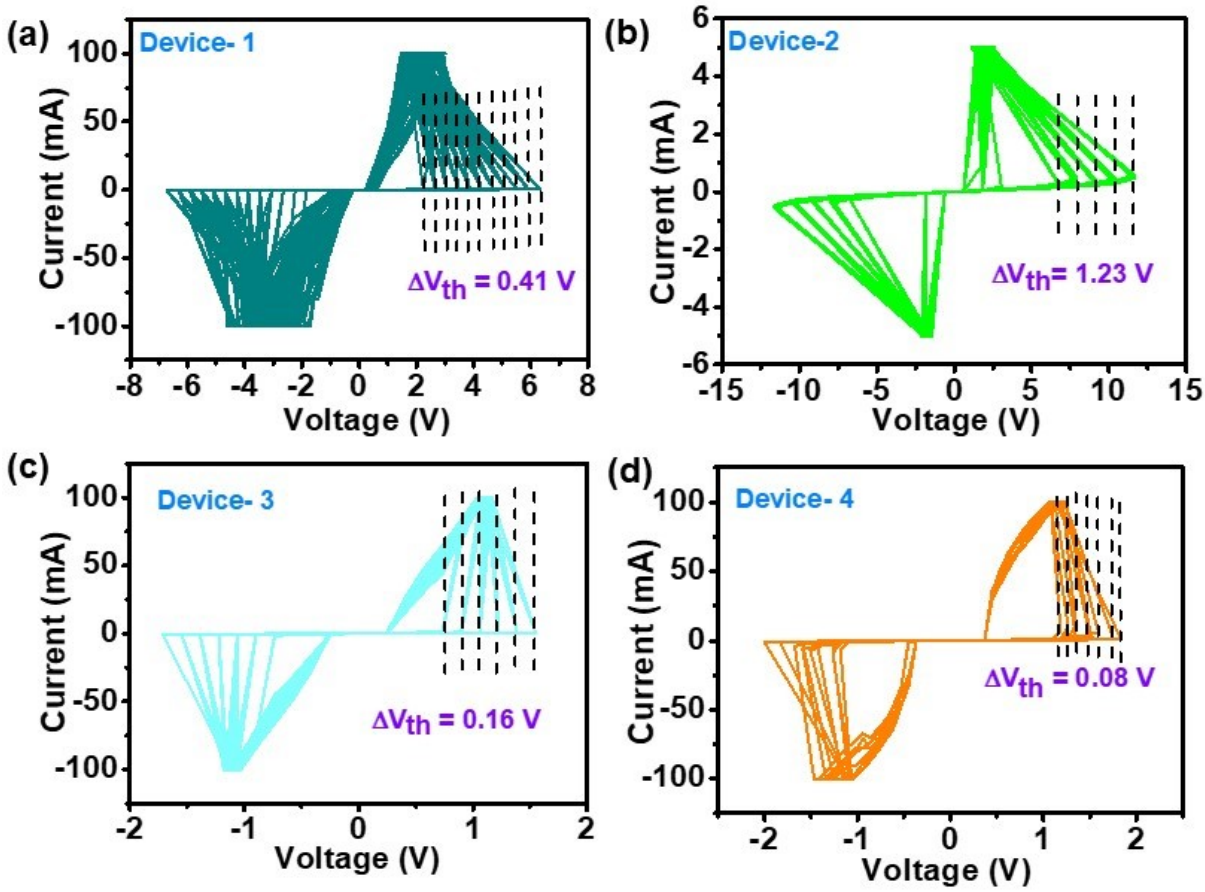

Figure S2. I-V measurements of various VO_2 crystal devices. (a-d) Device-1 to Device-4.

From figure S2 the statistics on threshold voltage distribution over their respective repeated I-V cycles is provided in below tables.

Figure S2a

N total	Mean	Standard Deviation	Minimum	Maximum
100	4.5988	1.1293	2.24	6.32

Figure S2b

N total	Mean	Standard	Minimum	Maximum

		Deviation		
100	9.69	1.28111	6.73	11.63

Figure S2c

N total	Mean	Standard Deviation	Minimum	Maximum
100	1.2876	0.13577	1.06	1.71

Figure S2d

N total	Mean	Standard Deviation	Minimum	Maximum
9	1.45222	0.25119	1.1	1.83

The actual ΔV_{th} values for all four devices are as follows 0.41 V, 1.23 V, 0.16 V and 0.08 V respectively. The ΔV_{th} values are measured between consecutive threshold switching cycles.

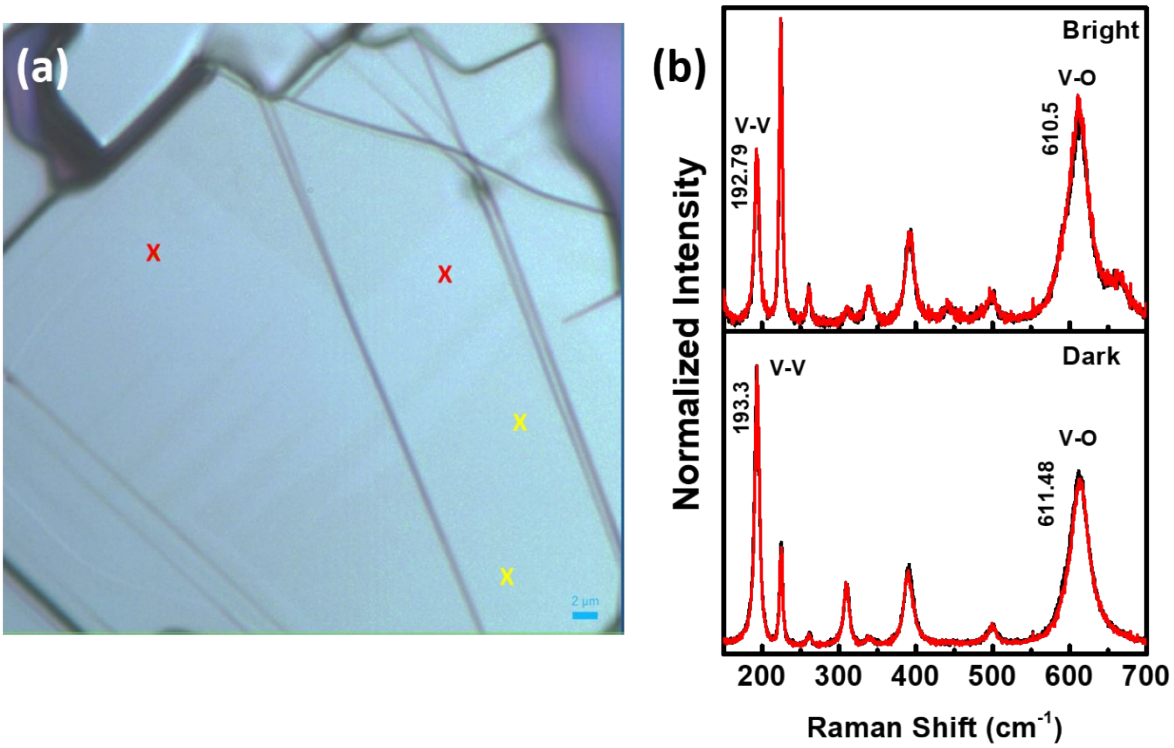

Figure S3. (a) Optical microscope image of VO_2 with bright and dark contrasts and (b) Raman spectra obtained from four neighbouring bright and dark regions of single crystal VO_2. The positions where the Raman spectrum was taken are marked with cross marks. The red cross marks correspond to bright, and the yellow corresponds to dark regions.

Figure S3a shows the surface morphology of single crystal VO_2 microplates grown on a quartz substrate. It is visible that as-grown microplates are distributed with bright and dark patterns randomly oriented without having any preferential orientations and controlled sizes. The Raman spectrum was collected using a 633 nm laser at room temperature as shown in Figure S3b. The Raman modes exhibiting vibrations at lower wave numbers correspond to V-V vibrations, while modes with higher wave numbers correspond to V-O vibrations[1].

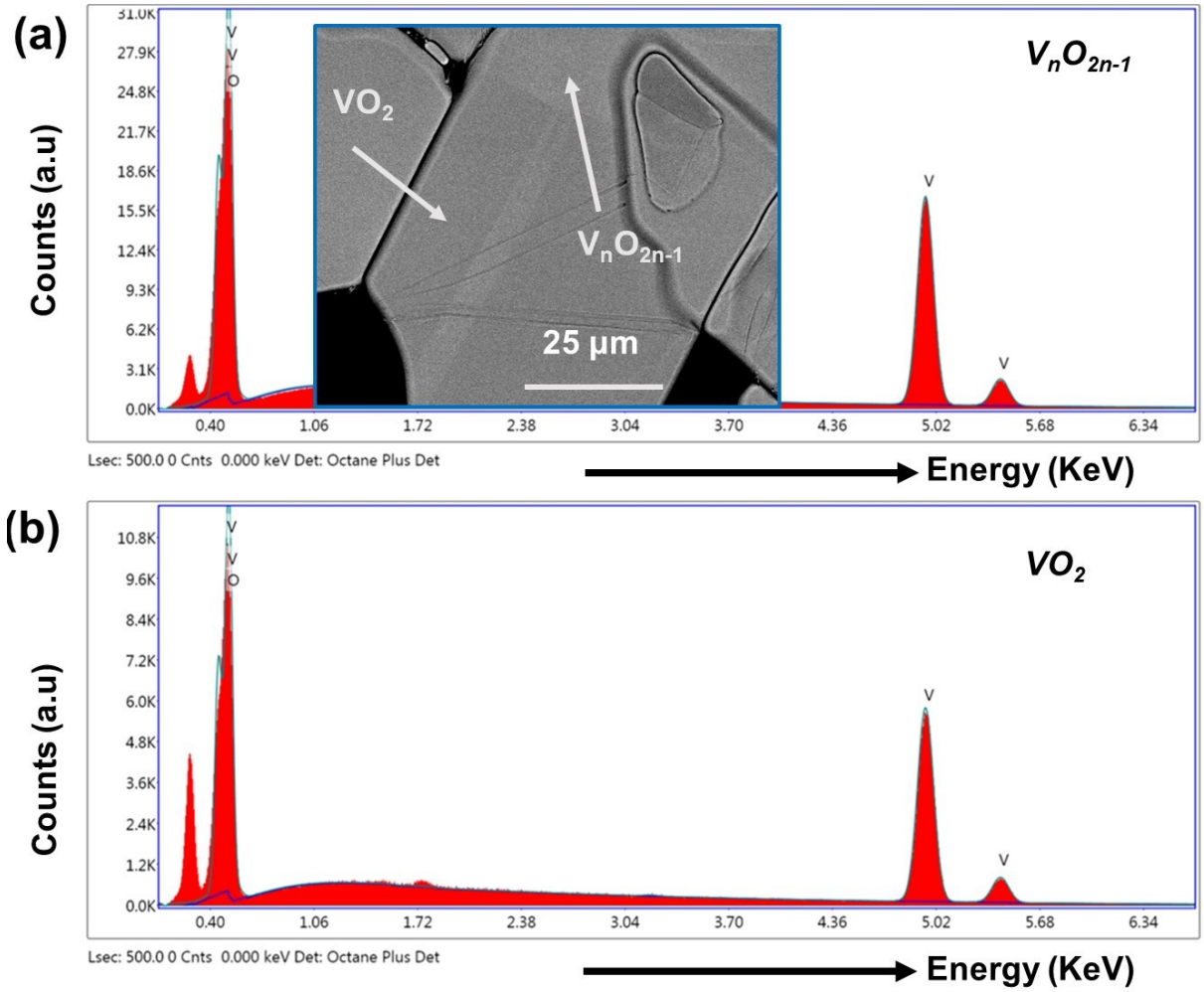

Figure S4. Energy dispersive x-ray spectroscopy (EDS) spectra from dark and bright regions of a VO_2 single crystal. It shows that V_nO_{2n-1} (bright region) intensity is nearly double the intensity of VO_2 (dark region).

The observed EDS spectral intensities showed a difference between dark and bright regions of the single crystal VO_2. The inset figure from Figures S4a and S4b shows the crystal from which spectra were collected. The results indicate minor variations in the composition between bright and dark regions of VO_2, suggesting the possible heterogeneity in the sample. We performed a point spectral analysis in bright and dark regions at six locations. From the obtained V and O atomic percentages, we compared V/O atomic percent ratios in bright (3.16 %) and dark regions (2.68 %). The low atomic percent (dark region) could be attributed to the VO_2 and high atomic percent (bright region) could be attributed to the VnO_{2n-1}.

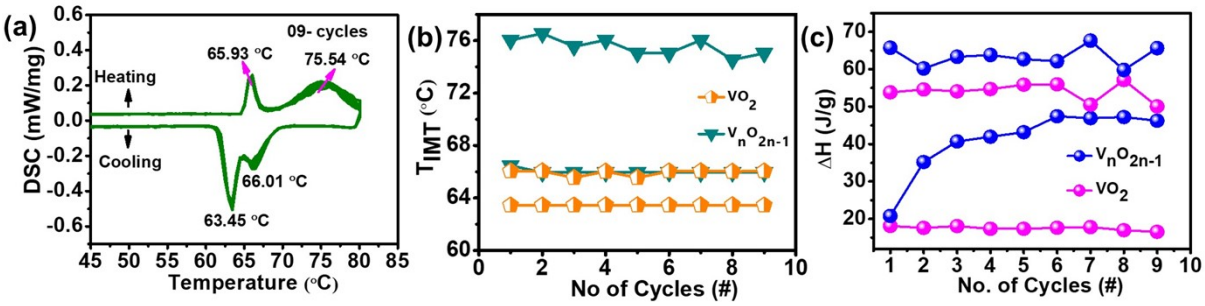

Figure S5. Differential scanning calorimetry (DSC) phase transition temperature analysis (a) DSC phase transition temperature plots. (b) IMT temperatures were recorded over 09 repeated cycles. Orange-coloured pentagons show IMT temperatures of VO_2, and dark cyan colour triangles represent VnO_{2n-1}. (c) enthalpy changes as a function of a number of cycles.

Pristine VO_2 is known for its structural phase transition at ~68 °C, DSC was performed to verify this further for our single crystal samples. The temperature range was chosen from 25 °C to 80 °C, and the scanning rate was set to 2 °C/min. The DSC shows two peaks in heating (at 65.93 °C and 75.54 °C) and two extremes in cooling (at 63.4 °C and 66.0 °C) mode respectively as shown in Figure S5a. To verify the reversibility of the phase change, we repeated the DSC nine times, and it is reproducible with a standard deviation of 65.9 ± 0.2 °C, 75.5 ± 0.6 °C in heating, and 63.4 ± 0.01°C and 66.01 ± 0.1 °C in cooling. Figure S5b shows the variation in insulator-metal transition temperature (T_{IMT}) as a function of number of cycles. Figure S5c shows the enthalpy change for phase transition as a function of number of cycles. Typically, stoichiometric VO_2 (M1) crystals show the phase transition at around 68° C in heating and 63 ° C in cooling. In contrast, in our study, slight changes in transition temperatures were observed due to chemical heterogeneity. Earlier reports, few factors like chemical doping[2], oxygen vacancies[3], and strain[4] are known to influence the T_{IMT}.

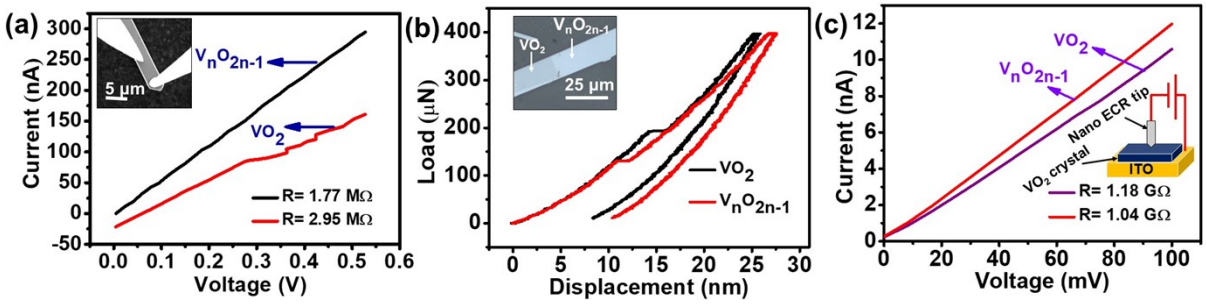

Figure S6. (a) *In-situ* SEM I-V plots of single crystal from VO_2 and V_nO_{2n-1} regions. (b) load-displacement plots from V_nO_{2n-1} and VO_2 region, for fixed 400 µN load. (c) I-V plots from nano ECR measurement conducted on VO_2 in vertical geometry.

By using *in-situ* SEM, we have conducted two probe I-V measurements locally in a planar geometry with the use of manipulators, as shown in Figure S6a. From the slopes of the linear I-V curves, we obtained a resistance of 2.95 MΩ in the dark region and 1.77 MΩ in the bright area. To further confirm the phase mixture via physical properties, we have performed site-specific nanoindentation using Hysitron triboindenter 950I. Load displacement curves for dark and bright regions are depicted in the Figure S6b. Reduced modulus for the dark region is 151.9± 6.2 GPa, while that for the bright part is 143.5 ± 1.9 GPa. While the average value of elastic modulus matches with the monoclinic phase of VO_2, the observed variation in elastic modulus values within the VO_2 crystals is significantly high[5]. The reduced modulus values clearly show that the mechanical properties of both regions are different and might be related to either coexisting phases or chemical heterogeneity. The hardness values for both areas were comparable, with dark (9.05 ± 0.22 GPa) slightly harder than the bright region (8.73 ± 0.15 GPa). The change in elastic modulus within the single crystal may be due to the compositional variation between the dark and bright regions as confirmed by EDS as presented in Figure S4.

To perform site-specific out-of-plane measurements, VO_2 crystals were transferred to conducting ITO substrate using a scotch tape. For site specific, I-V measurements, bright and dark regions were identified with the help of an optical microscope, then nanoECR technique was used to measure the out-of-plane electrical behaviour of the VO_2 crystals. A schematic of

the measurement setup is shown in the right side inset of Figure S6c. Voltage sweep within a range of -100 mV to 100 mV was performed during the holding period. The represented linear curves show a resistance of 1.18 GΩ and 1.04 GΩ in VO_2 and V_xO_y regions, respectively. It is important to note that the nanoECR measurements in vertical geometry show much higher resistance due to the increased contact resistance between the physically transferred VO_2 crystal and ITO. Nevertheless, electrical measurements from in-situ SEM and nano ECR indicate that the VO_2 crystal contains specific level of heterogeneity, and the VO_2 region has a higher resistance than V_nO_{2n-1}.

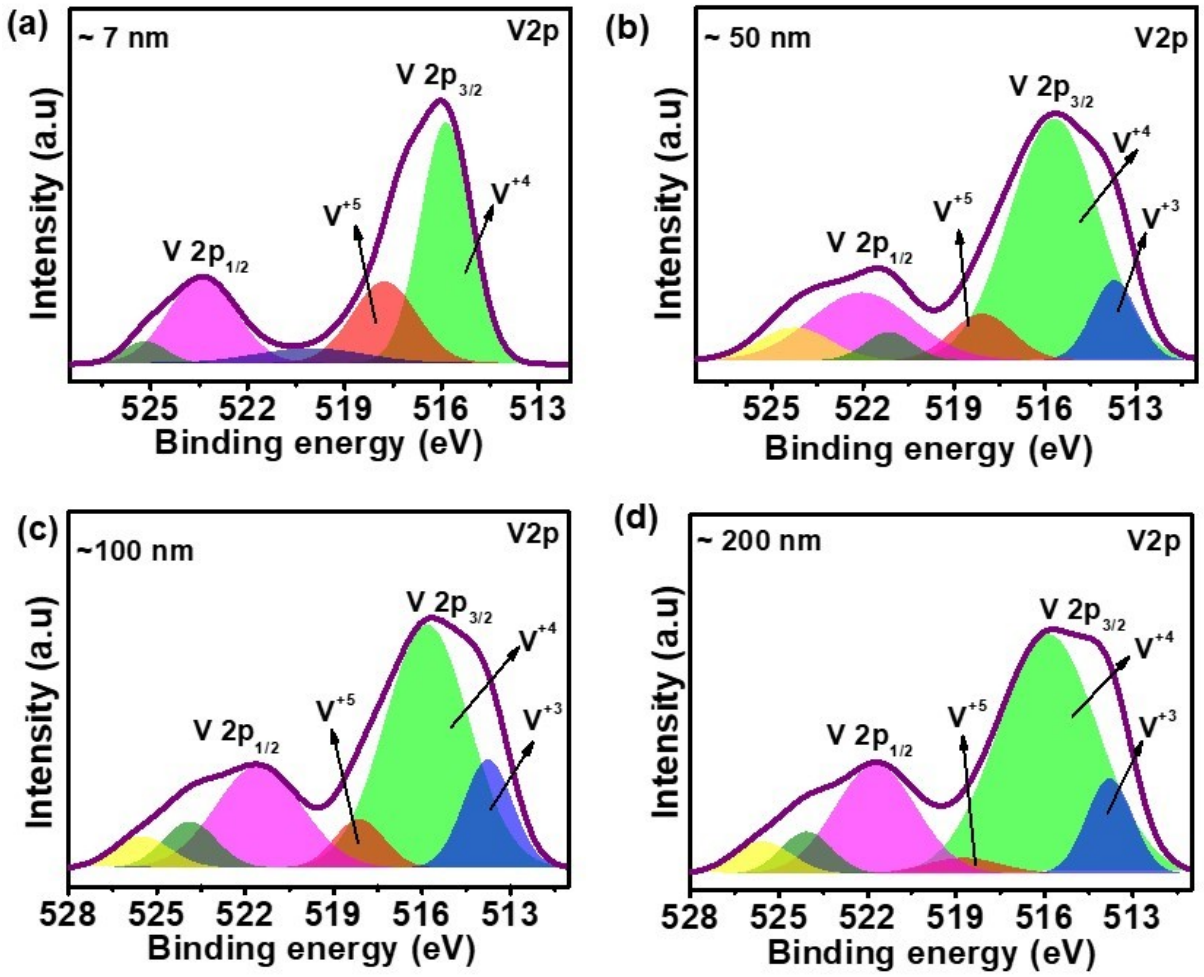

Figure S7. XPS V2p spectra depth analysis for different etching values of (a) 7 nm (b) 50 nm (c) 100 nm and (d) 200 nm respectively.

The deconvolution of V2p spectra are presented in Figure S7. At the top surface, peaks at 515.8 eV and 517.7 eV are assigned to V+4 and V+5 oxidation states respectively according to NIST data base. As we delve deeper into the crystal, +3 (513.7 eV) and +4 (515.8 eV) states dominant and +5 oxidation states almost diminishes.

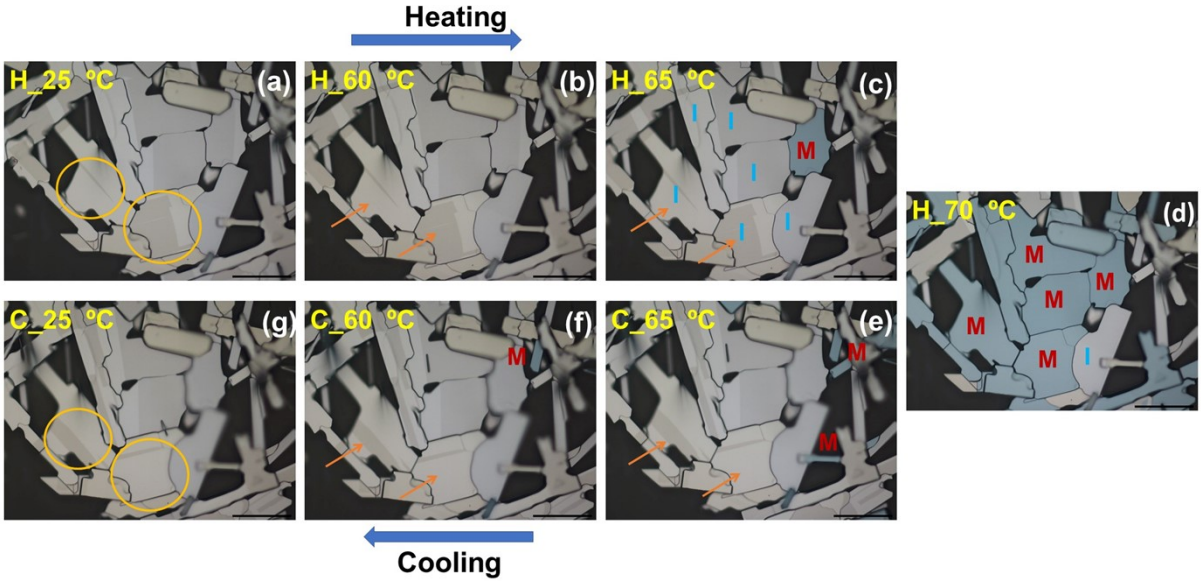

Figure S8. Optical microscopy images of single crystal VO_2 for studying the thermal heating and cooling effect on chemical heterogeneity dynamics. Metallic and insulating domains are marked with the letters "M" and "I," respectively, near the transition temperature. Orange-coloured circled regions are interesting observations for bright and dark regions' motion at 25ºC, well below the transition temperature.

Figure S8 shows random bright and dark patterns at room temperature. This intriguing pattern behavior of VO_2 crystals changes their dynamics during heating and cooling. This is noticeable in Figure S8a & g. The dark pattern in the small circle and big circle change drastically during cooling, and similar observations are also made in Figure S8b & f and Figure S8c & e. At elevated temperature above IMT temperature, most of the crystals start turning into a complete metallic state (Figure S8d). The observed bright and dark contrast at room temperature and

their domain dynamics may be caused by variations in chemical heterogeneity across crystals facilitated by their non-stoichiometry.

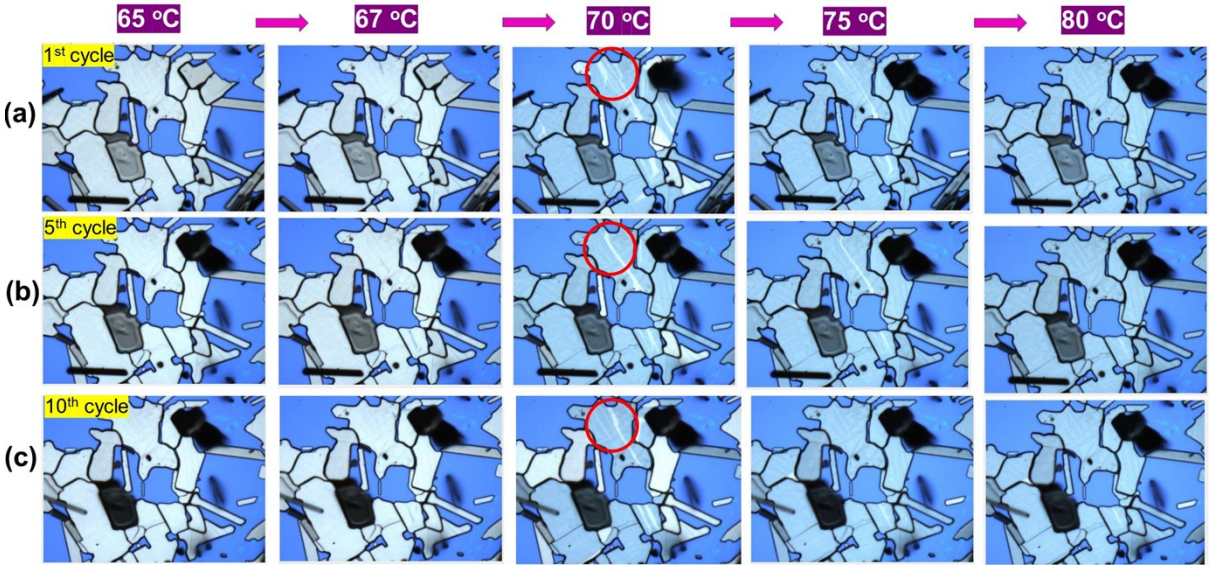

Figure S9. Optical microscopy images of single crystal VO_2 under heating conditions, showing dynamics in IMT domains.

From figure S9 single crystal optical images, it is evident that single crystal VO_2 shows distinct optical contrasts under microscopy. To record the real-time domain wall dynamics, optical images were recorded while heating the sample to a temperature near and above the IMT temperatures like 65 ^{o}C, 70 ^{o}C, 75 ^{o}C, 80 ^{o}C and 85 ^{o}C from room temperature. Experiments were done by placing a heating stage under a microscope, and heating was supplied with a ramp rate of 2 ^{o}C/min, and during cooling, it is allowed for natural cooling. Figure S9a shows the optical images of single crystal VO_2 with pale yellow colour for insulator phase and sky-blue colour for metallic region, which is consistent with other reports elsewhere[6]. Figure S9b-c shows the 5th and 10th repeated heating and cooling cycles. White, there is slight lagging between the contrast variations during heating and cooling; there are no observable changes across the phase transition temperature. On the contrary, the bright and dark contrasts at room temperature show some variations, indicating the variation in the chemical heterogeneity.

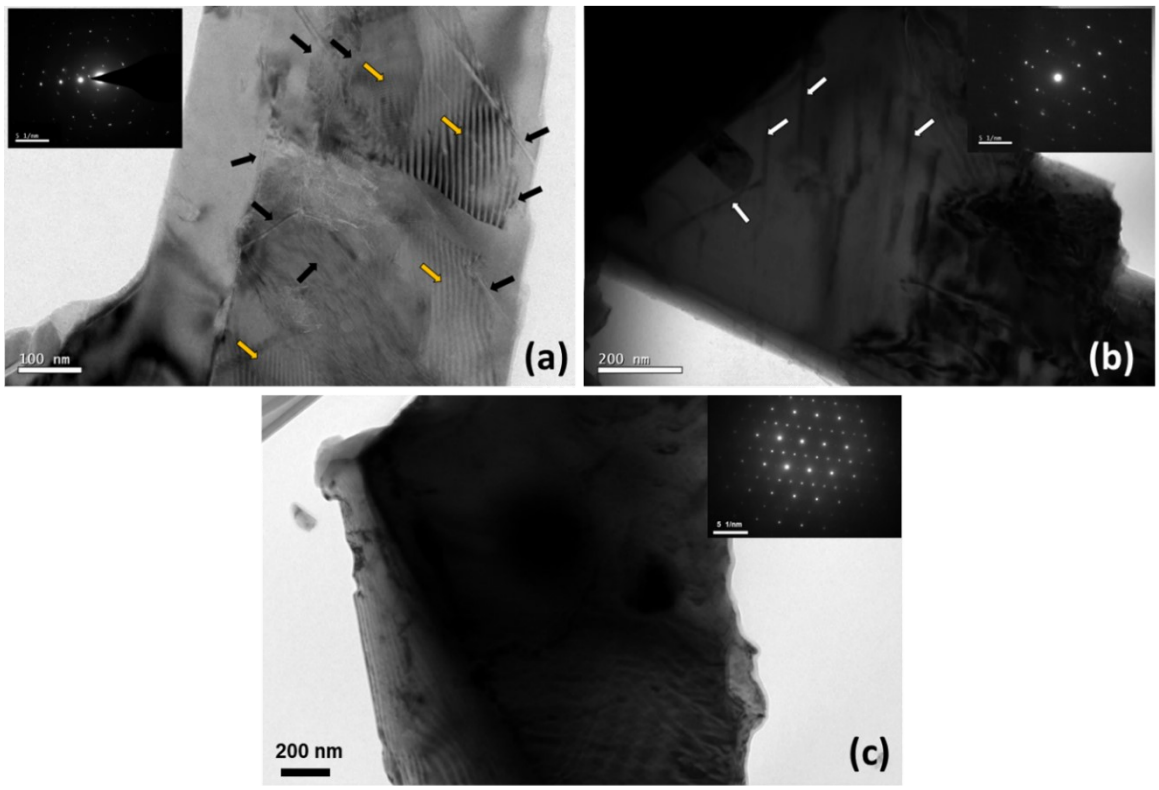

Figure S10. The TEM bright field images and selected area electron diffraction pattern of VO_2 crystal in the inset. (a) The lamellar-like microstructure was indicated by black arrow marks and moiré fringes marked with yellow arrows. (b) Microdomain-like line contrasts are marked with white arrow marks. (c) Thick VO_2 platelet. Selected area electron diffraction patterns shown in insets comprise superlattice reflections from nonstoichiometric V_nO_{2n-1} phases.

TEM investigations revealed lamellar structures consisting of microdomains and moiré patterns within the VO_2 single crystals, as shown in Figure S10(a). In particular, the formation of moiré patterns indicates the overlapping layers of two different phases, possibly VO_2 and V_nO2_{n-1}. The systematic loss of oxygen in vanadium oxide results in forming the Magnéli structure, V_nO_{2n-1}, where the "n" can be directly related to the superlattice formation by introducing crystallographic shear in specific planes. Such arrays of superlattice reflections are evident from the electron diffraction pattern in Figure S10(b-c).

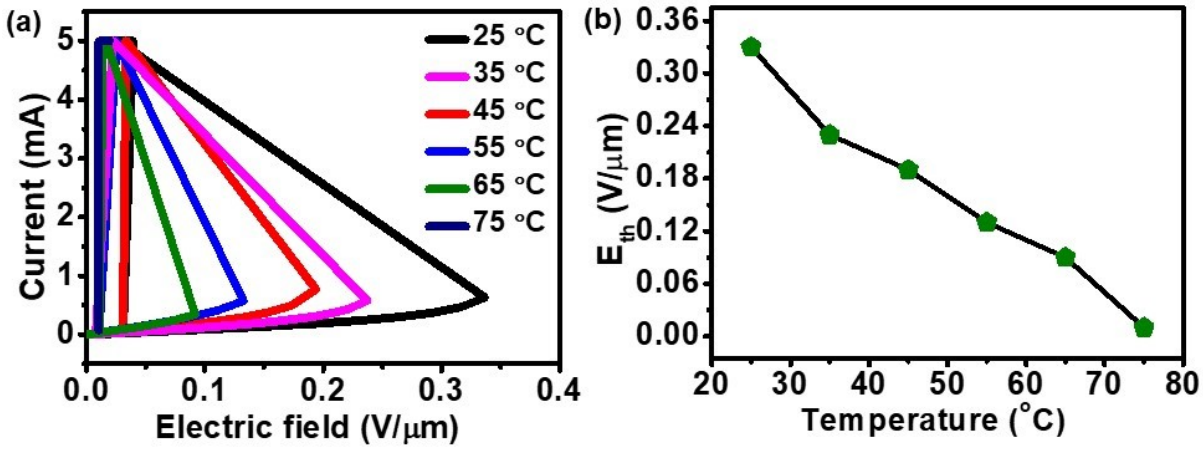

Figure S11. (a) Current as a function of electric field at different temperatures (b) The electric field threshold dependence on temperature.

We have performed a simple measurement to comment on unavoidable presence of IMT effect in our sample. This suggests that if the conduction mechanism is dominated by VO_2 IMT behaviour, then at temperatures above 68°C, we will not see any threshold switching behaviour; instead, we will observe linear behaviour. Hence the observed resistive switching rests upon VO_2's widely recognized structural / electronic phase transition at 68°C. As anticipated, with increasing temperature, the E_{th} values decreases, and beyond 68°C, VO_2 transitions into a metallic state as shown in figure S11 (a & b).

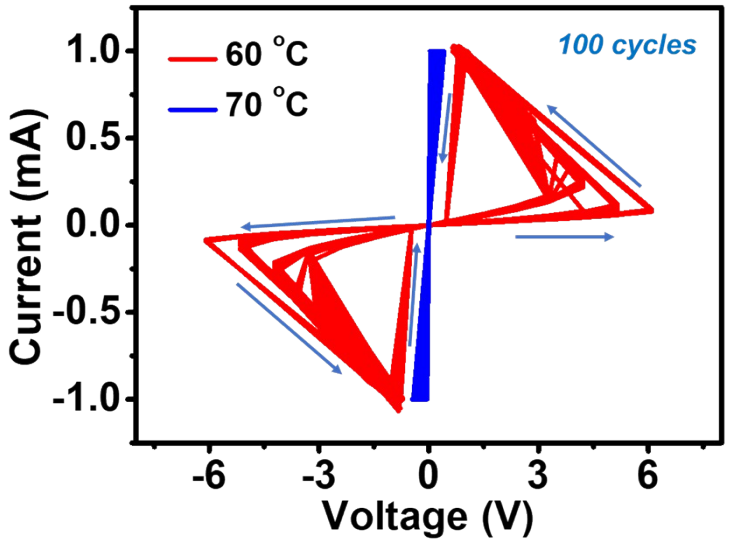

Figure S12. Current-voltage plots are depicted in red and blue for temperatures just below and just above the phase transition, respectively.

We performed temperature-dependent I-V measurements over 100 cycles at temperatures below and above the VO_2 phase transition temperature as shown in figure S12.

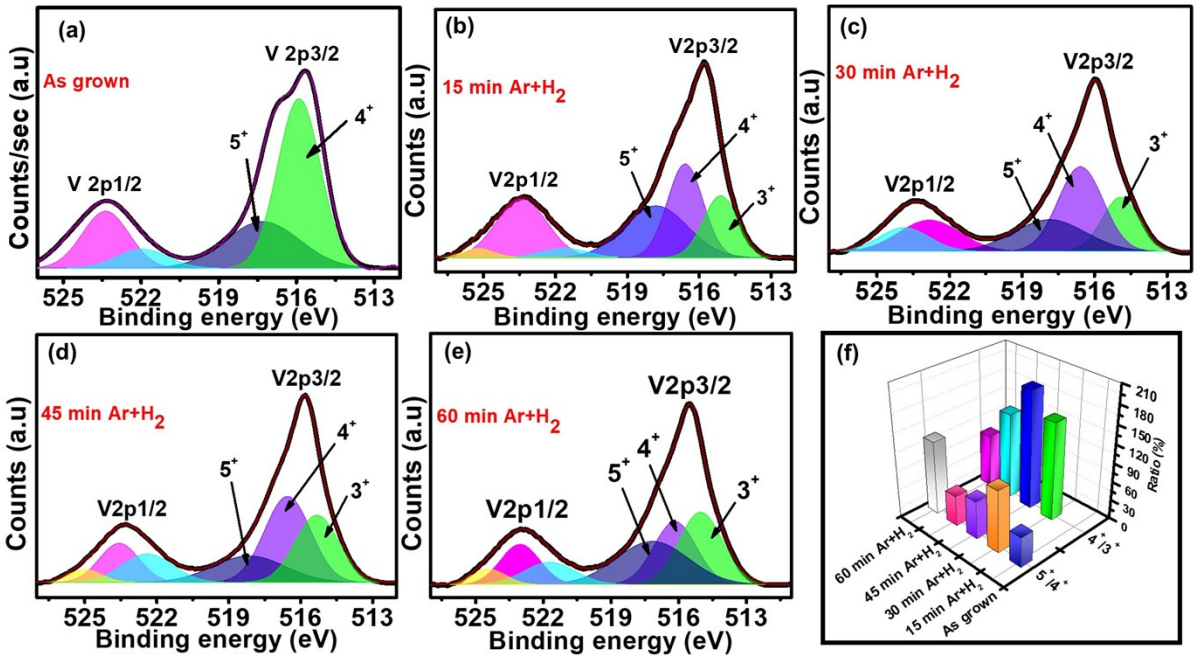

Figure S13. Depicts the XPS characterization of the Ar+H_2 annealed crystalline VO_2 sample. V2p spectra for (a) as grown VO_2 having +4 and +5 oxidation states (b) 15 min Ar+H_2 annealed sample with +3, +4 and +5 oxidation states (b) 30 min Ar+H_2 annealed sample with +3, +4 and +5 oxidation states (c) 45 min Ar+H_2 annealed sample with +3, +4 and +5 oxidation states (d) 60 min Ar+H_2 annealed sample with +3, +4 and +5 oxidation states and (e) 3D histogram representing distribution of oxidation state percentages from each sample.

The XPS spectra in Figures S13a-e show the V 2p fitting for as-grown and Ar+H_2 annealed samples, with binding energies corrected using the adventitious carbon C1s binding energy of 284.8 eV. The V $2p_{3/2}$ spectrum of the as-grown VO_2 sample was deconvoluted into two peaks corresponding to +4 and +5 oxidation states, while the annealed samples were deconvoluted into three peaks corresponding to +3, +4, and +5 oxidation states. Figure S13f presents the histogram distribution of the atomic percentages of these various oxidation states. The as-grown VO_2 crystalline sample exhibits 67.6 at. % of the +4 oxidation state (i.e. pure VO_2) and 32.3 at. % of the +5 oxidation state (V_2O_5). In the annealed samples, the +3 oxidation state appears along with +4 and +5 oxidation states and its atomic percentage increases steadily from 24.5% to 35.2% with increasing annealing time from 15 minutes to 60 minutes. However, there is no consistent trend is observed in the +4 and +5 oxidation states of annealed samples. From

XPS analysis it infers that with increasing annealing time there is increase in +3 oxidation state which is oxygen deficient (V_2O_3) phase of VO_2. To develop a mechanistic understanding, systematic electrical measurements were carried out on post growth annealed VO_2 samples and compared with as grown VO_2 samples (Figure S14). Since structural stability and IMTs are highly influenced by oxygen deficiencies, resistance versus temperature measurements were performed to analyze their effects on transition temperature and resistance changes (Figure S14a). The as-grown VO_2 crystal shows a resistance change of 554 (Resistance change = $R_{(Insulator)}$ / $R_{(Metal)}$ from its insulating to metallic state, and the IMT temperature (T_{IMT}) is about 64°C, which is 4°C lower than the actual stoichiometric VO_2 ($T_{IMT} \approx 68°C$). The possible reason for the lower IMT could be oxygen nonstoichiometric in VO_2. Since our electric field-dependent stochasticity is only in SET voltages, we performed our RT plots only in heating mode. Post-growth annealing was performed under Ar+H_2 gas for different durations, ranging from 15 minutes to 60 minutes, in 15-minute intervals. The annealed samples show T_{IMT} of 67°C, 65°C, 66°C, and 67°C, and varying orders of resistance change from 120, 233, 114, and 20 for the 15-minute to 60-minute annealed samples, respectively. The deviations in phase transition temperatures and changes in transition order suggest the influence of oxygen vacancies during annealing. Oxygen vacancies are sensitive to both thermal and electrical measurements, and our I-V plots show stochastic switching in both as-grown and all annealed samples with discrete stochastic switching, as shown in Figure S14(b-f). The current-voltage characteristics of the annealed samples result in a reduced number of transition points (V_{th}) compared to the multiple discrete V_{th} observed in the as-grown samples. The discrete V_{th} features observed in both as-grown and post-annealing treated samples were analyzed based on the dynamics of oxygen deficiencies under electric fields. From the XPS analysis, it suggests that reducing multiple discrete stochastic switching points in annealed samples could be due to increase in V_2O_3 content in VO_2 and V_2O_5 mixed phases.

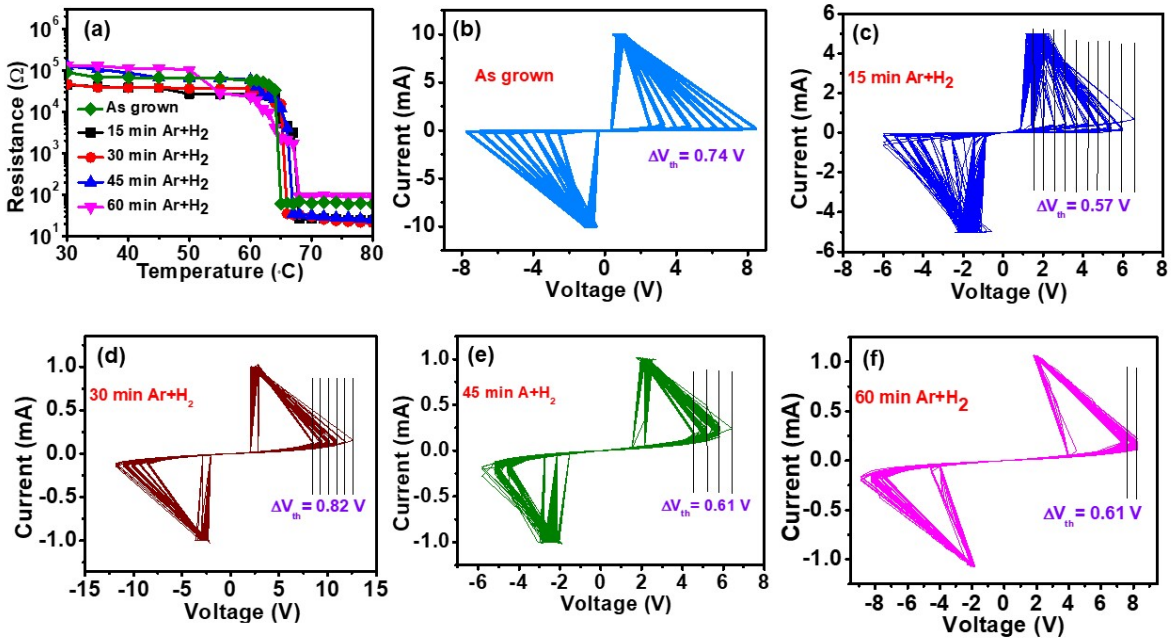

Figure S14. Depicts the RT plots and discrete I-V switching curves. (a) RT plots for a as grown and different Ar+H_2 annealed time dependent samples under heating mode. I-V switching characteristics for (a) as grown samples with a multiple discrete stochastic switching having equal ΔV_{th} of 0.74 V (b) 15 min- Ar+H_2 annealed sample (c) 30 min Ar+H_2 annealed sample (d) 45 min Ar+H_2 annealed sample and (e) 60 min Ar+H_2 annealed sample with higher number of discrete thresholds switching to reduced number of discrete switching having different ΔV_{th} voltages.

The number of discrete electrical switching points is quite high in as-grown and post-annealing 15-minute samples, and those switching points decrease as annealing time increases. In addition to discrete switching points, it has been found that each individual sample's voltage difference (ΔV_{th}) between subsequent SET voltages remained consistent.

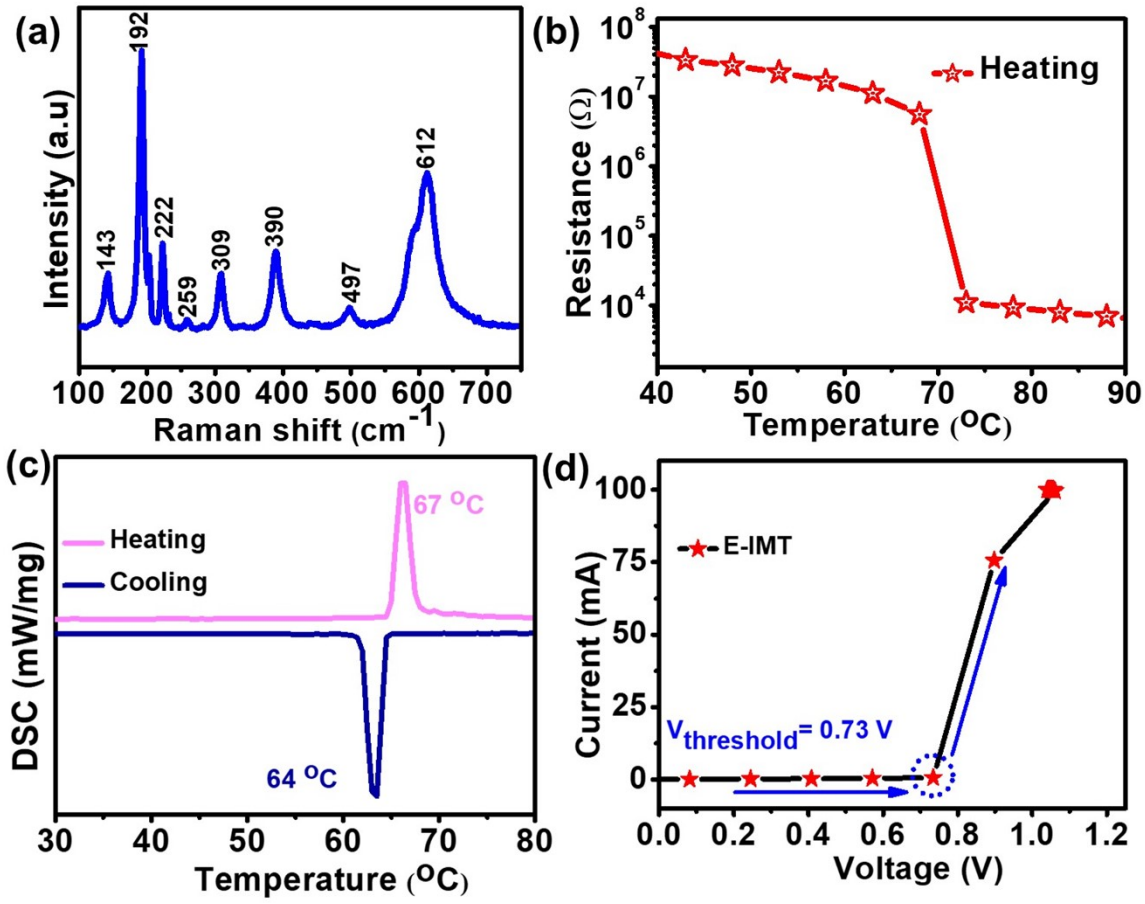

Figure S15. Raman spectrum and the phase transition confirmation in polycrystalline VO_2. (a) Raman spectrum of PC-VO_2 (b) Thermal triggering of insulator-metal phase transition captured via R-T plot during heating (c) DSC confirmation for phase change in VO_2 (d) Electrical triggering induced phase change.

Figure S13a shows the Raman spectrum of the PC-VO_2 and all the vibrational modes are consistent with VO_2 modes. Figure S13b shows the resistance versus temperature (RT) plot of polycrystalline VO_2. In the heating mode, more than three orders of resistance change were observed, and the recorded IMT temperature is ~ 69 °C. Further the phase transition temperature of VO_2 polycrystalline samples was investigated by differential scanning calorimetry (DSC). The typical IMT in the sample exhibits a heating peak of about ~ 67 °C during the endothermic process and a cooling peak of about ~ 64 °C during the exothermic process, as shown by the DSC curves in Figure S13c. Figure S13d shows the electrically induced IMT with a low threshold voltage of 0.73 V in planar device geometry. The

comparison between orders of resistance change suggests the R_T is approximately 11 times higher than in R_E. Where, R_T is defined as the ratio between the resistance values in insulating (at 40 °C) and metallic state (at 90 °C) during thermal heating, showing a value of ~ 4,786 Ω. Similarly, the R_E is defined as the ratio between the resistance values in insulating (at 0.2 V) and metallic state (at 1 V), showing a value of ~ 416 Ω under electric field-induced IMTs.

Free energy Calculation:

We have used conventional chemical thermodynamics to estimate the Gibbs free energy using Nernst equation for electrochemical reactions in VO_2. In the present case, the electrochemical reactions are triggered by electric field and results in the formation of series of non-stoichiometric, Magnéli phases wherein valence states of vanadium and charge transfer is fractionalised as the O/V ratio is varied. The qualitative free energy charges along with corresponding parameters are presented in Table 1. The details of free energy calculations for the formation of different reactions for non-stoichiometric, Magnéli phases are also presented.

S. No	Composition x in VO_x	Charge Transfer (z)	n	Phase	E	ΔG (kJ/mole)
1	1.5	1	2	V_2O_3	0.3105	-29.96
2	1.66	0.67	3	V_3O_5	0.2960	-19.13
3	1.75	0.5	4	V_4O_7	0.281	-13.55
4	1.8	0.4	5	V_5O_9	0.2663	-10.27
5	1.83	0.34	6	V_6O_{11}	0.2533	-8.31
6	1.85	0.29	7	V_7O_{13}	0.2383	-6.66
7	1.87	0.25	8	V_8O_{15}	0.222	-5.35
8	1.88	0.22	9	V_9O_{17}	0.206	-4.37
9	1.9	0.2	10	$V_{10}O_{19}$	0.1925	-3.71
10	1.909	0.18	11	$V_{11}O_{21}$	0.1762	-3.06

Table S1. The estimated values of change in free energy with respect to composition of vanadium oxides and respective parameters, used in redox reaction.

It has been reported that the Wadsley phase (V_nO_{2n+1}) of vanadium oxide can exhibit fractional valence, resulting in the formation of a specific Wadsley phase[13]. The free energy plots as a function of fractional charges in vanadium oxide for Wadsley phase (V_nO_{2n+1}) shows discrete step like behaviour[14]. In other systems such as TiO_2, free energy calculations have been reported for Magnéli phase, but they utilized parameters such as partial pressure of oxygen and temperature to stabilize the non-stoichiometric phases and shown that the free energies are discretised when the compositions are varied. In contrast, all of our experiments were conducted near room temperature, and the Magnéli phase changes were induced by an electric field stimulus. In consideration of the aforementioned views, we conducted qualitative estimations for the Magnéli phases of VO_2 with the use of fractional valences as the O/V ratio is varied.

For all the reactions involving the formation of Magnéli phase from VO_2, the expression can be simplified as follows.

For example,

$$2VO_2 \rightarrow V_2O_3 + \frac{1}{2}O_2 \text{ ---------- (1)}$$

$$K = \frac{[V_2O_3][O_2]^{1/2}}{[VO_2]^2} \text{ ---------- (2)}$$

$$K = \frac{1}{2}P(O_2) \text{ ---------- (3)}$$

The above value of K is valid for all other reaction with the formations of V_2O_3, V_3O_5, V_4O_7, V_5O_9. By substituting the value of K, equation (3) in equation (1)

$$E = E^o - \frac{2.303\,RT}{ZF}\frac{1}{2}P[O_2]$$

E= E^o- $\frac{2.303\,RT}{ZF}\frac{1}{2}$; where, $P[O_2] = 1\ atm$

E= E^o- $\frac{1.1515}{ZF}$ RxT ---------- (1)

Assuming the same E^o value of 0.34 for all reactions (1 electron transfer) involving fractional charge transfer.

R= 8.314; T= 298 K; and F= 96500

E= 0.34- $\frac{1.1515x8.341x298}{Zx96500}$

E= 0.34- $\frac{0.0295}{Z}$ ----------(2)

E= E^o- $\frac{0.0295}{Z}$ ----------(3)

For charge transfer of one (or fractional charges), E^o = 0.34 is assumed to be constant. For reduction of $V^{+4} \rightarrow V^{+3}$ and to form possible Magnéli phases, the following reactions are considered. Typically, Nernst equation is used for electrochemical reactions involving charge transfer in integers. For example, the formation of V_2O_3 from VO_2 involves a charge transfer of 1 as the valence changes from +4 to +3. However, formation of other non-stoichiometric phases such as V_3O_5, V_4O_7, etc. involves fractional charge transfer (Z= 0.67 & Z= 0.5) as the valence takes the fractional values (3.33 & 3.5). This is due to the fact that such non stoichiometric phases evolve as we increase the oxygen vacancy concentration. Such fractional charges for vanadium is reported in Wadsley phases as well[13].

(i). $2VO_2 \rightarrow V_2O_3 + \frac{1}{2}.O_2$; [O/V= 1.5; V^{+3}; Z=1]

(ii). $3VO_2 \rightarrow V_3O_5 + \frac{1}{2}.O_2$; [O/V= 1.66; $V^{+3.33}$; Z=0.67]

(iii). $4VO_2 \rightarrow V_4O_7 + \frac{1}{2}.O_2$; [O/V= 1.75; $V^{+3.5}$; Z=0.5]

(iv). $5VO_2 \rightarrow V_5O_9 + \frac{1}{2}.O_2$; [O/V= 1.8; $V^{+3.6}$; Z=0.4]

(v). $6VO_2 \rightarrow V_6O_{11} + \frac{1}{2}.O_2$; [O/V= 1.83; $V^{+3.66}$; Z=0.34]

(vi). $7VO_2 \rightarrow V_7O_{13} + \frac{1}{2}.O_2$; [O/V= 1.85; $V^{+3.71}$; Z=0.29]

(vii). $8VO_2 \rightarrow V_8O_{15} + \frac{1}{2}.O_2$; [O/V= 1.875; $V^{+3.75}$; Z=0.25]

(viii). $9VO_2 \rightarrow V_9O_{17} + \frac{1}{2}.O_2$; [O/V= 1.88; $V^{+3.777}$; Z=0.22]

(ix). $10VO_2 \rightarrow V_{10}O_{19} + \frac{1}{2}.O_2$; [O/V= 1.9; $V^{+3.8}$; Z=0.20]

When Z=1;

$E = 0.34 - 0.0295 \Rightarrow 0.3105$;

$\Delta G = -ZFE = -1x96.5x0.3105 = -29.96$ KJ/mol

Where,

ΔG: Change in Gibbs free energy (units: Joules (J) or kilojoules per mole (kJ/mol)) – at constant temperature and pressure.

Z: Number of electrons transferred per mole of reaction (unitless).

F: Faraday's constant (approximately 96485 C/mol) - This is a fundamental constant that relates the amount of electrical charge to the number of electrons involved in a reaction.

E: Cell potential (units: Volts (V)) - This represents the voltage produced by the device.

When Z=0.67;

E= 0.34- 0.0440⇒0.2960; ΔG= -ZFE= -0.67x96.5x0.296 = -19.13 KJ/mol

When Z=0.5;

E= 0.34- 0.0590⇒0.281; ΔG= -ZFE= -0.5x96.5x0.281 = -13.55 KJ/mol

When Z=0.4;

E= 0.34- 0.0737⇒0.2663; ΔG= -ZFE= -0.4x96.5x0.2663 = -10.27 KJ/mol

When Z=0.34;

E= 0.34- 0.0867⇒0.2533; ΔG= -ZFE= -0.34x96.5x0.2533 = -8.31 KJ/mol

When Z=0.29;

E= 0.34- 0.1017⇒0.23833; ΔG= -ZFE= -0.29x96.5x0.2353 = -6.66 KJ/mol

When Z=0.25;

E= 0.34- 0.118⇒0.222; ΔG= -ZFE= -0.25x96.5x0.222 = -5.35 KJ/mol

When Z=0.22;

E= 0.34- 0.1340⇒0.206; ΔG= -ZFE= -0.22x96.5x0.206 = -4.37 KJ/mol

When Z=0.20;

E= 0.34- 0.1475⇒0.1925; ΔG= -ZFE= -0.29x96.5x0.1925 = -3.71 KJ/mol

References

(1) Shvets, P.; Dikaya, O.; Maksimova, K.; Goikhman, A. A Review of Raman

Spectroscopy of Vanadium Oxides. *J. Raman Spectrosc.* **2019**, *50* (8), 1226–1244. https://doi.org/10.1002/jrs.5616.

(2) Naik B., R.; Verma, D.; Balakrishnan, V. Effect of Chemical Doping on Memristive Behavior of VO2microcrystals. *Appl. Phys. Lett.* **2022**, *120* (6). https://doi.org/10.1063/5.0075566.

(3) Jeong, J.; Aetukuri, N.; Graf, T.; Schladt, T. D.; Samant, M. G.; Parkin, S. S. P. Suppression of Metal-Insulator Transition in VO2 by Electric Field-Induced Oxygen Vacancy Formation. *Science (80-.).* **2013**, *339* (6126), 1402–1405. https://doi.org/10.1126/science.1230512.

(4) Kim, H.; Charipar, N. A.; Figueroa, J.; Bingham, N. S.; Piqué, A. Control of Metal-Insulator Transition Temperature in VO 2 Thin Films Grown on RuO 2 /TiO 2 Templates by Strain Modification. *AIP Adv.* **2019**, *9* (1). https://doi.org/10.1063/1.5083848.

(5) Singh, D.; Viswanath, B. In Situ Nanomechanical Behaviour of Coexisting Insulating and Metallic Domains in VO2 Microbeams. *J. Mater. Sci.* **2017**, *52* (10), 5589–5599. https://doi.org/10.1007/s10853-017-0792-4.

(6) Shi, R.; Chen, Y.; Cai, X.; Lian, Q.; Zhang, Z.; Shen, N.; Amini, A.; Wang, N.; Cheng, C. Phase Management in Single-Crystalline Vanadium Dioxide Beams. *Nat. Commun.* **2021**, *12* (1), 1–9. https://doi.org/10.1038/s41467-021-24527-5.

(7) Palau, A.; Fernandez-Rodriguez, A.; Gonzalez-Rosillo, J. C.; Granados, X.; Coll, M.; Bozzo, B.; Ortega-Hernandez, R.; Suñé, J.; Mestres, N.; Obradors, X.; Puig, T. Electrochemical Tuning of Metal Insulator Transition and Nonvolatile Resistive Switching in Superconducting Films. *ACS Appl. Mater. Interfaces* **2018**, *10* (36), 30522–30531. https://doi.org/10.1021/acsami.8b08042.

(8) Zhang, J.; Zhao, Z.; Li, J.; Jin, H.; Rehman, F.; Chen, P.; Jiang, Y.; Chen, C.; Cao, M.; Zhao, Y. Evolution of Structural and Electrical Properties of Oxygen-Deficient VO2 under Low Temperature Heating Process. *ACS Appl. Mater. Interfaces* **2017**, *9* (32), 27135–27141. https://doi.org/10.1021/acsami.7b05792.

(9) Moatti, A.; Sachan, R.; Gupta, S.; Narayan, J. Vacancy-Driven Robust Metallicity of Structurally Pinned Monoclinic Epitaxial VO 2 Thin Films. *ACS Appl. Mater. Interfaces* **2019**, *11* (3), 3547–3554. https://doi.org/10.1021/acsami.8b17879.

(10) Sharma, Y.; Balachandran, J.; Sohn, C.; Krogel, J. T.; Ganesh, P.; Collins, L.; Ievlev, A. V.; Li, Q.; Gao, X.; Balke, N.; Ovchinnikova, O. S.; Kalinin, S. V.; Heinonen, O.; Lee, H. N. Nanoscale Control of Oxygen Defects and Metal-Insulator Transition in Epitaxial Vanadium Dioxides. *ACS Nano* **2018**, *12* (7), 7159–7166. https://doi.org/10.1021/acsnano.8b03031.

(11) Zhang, S.; Kim, I. S.; Lauhon, L. J. Stoichiometry Engineering of Monoclinic to Rutile Phase Transition in Suspended Single Crystalline Vanadium Dioxide Nanobeams. *Nano Lett.* **2011**, *11* (4), 1443–1447. https://doi.org/10.1021/nl103925m.

(12) Valov, I.; Linn, E.; Tappertzhofen, S.; Schmelzer, S.; Van Den Hurk, J.; Lentz, F.; Waser, R. Nanobatteries in Redox-Based Resistive Switches Require Extension of Memristor Theory. *Nat. Commun.* **2013**, *4*, 1–9. https://doi.org/10.1038/ncomms2784.

(13) Katzke, H.; Tolédano, P.; Depmeier, W. Theory of Morphotropic Transformations in Vanadium Oxides. *Phys. Rev. B - Condens. Matter Mater. Phys.* **2003**, *68* (2), 1–7. https://doi.org/10.1103/PhysRevB.68.024109.

(14) You, Z.; Jung, I. H. Critical Evaluation and Thermodynamic Optimization of the Fe-P System. *Metall. Mater. Trans. B Process Metall. Mater. Process. Sci.* **2020**, *51* (6), 3108–3129. https://doi.org/10.1007/s11663-020-01939-0.